

Divergent Impact Charging of Polymer Particles

Simon Jantač¹ and Holger Grosshans^{1,2,*}

¹*Physikalisch-Technische Bundesanstalt, Braunschweig, Germany*

²*Otto von Guericke University of Magdeburg, Institute of Apparatus and Environmental Technology, Magdeburg, Germany*

When a particle contacts a surface of another material, it is commonly believed that the particle acquires an impact charge that scales inversely with its pre-impact charge and whose polarity is set by the materials. We show that this belief holds for conductive particles but fails for polymers. For polymers, the impact charge increases linearly with the particle's pre-impact charge. Its polarity is not determined by the materials but by the pre-impact particle charge relative to a divergence point at which the net charge transfer reverses. We attribute this divergence to the attraction of surrounding ions to the particle surface. These attracted ions carry polarity opposite to that of the particle, and their amount scales with the particle charge. They transfer to the opposing surface during contact, thereby defining the impact charge. We propose a phenomenological model for the divergent impact charge arising from this mechanism. Finally, we reexamine previous measurements and show that they support this mechanism.

Contact electrification—the transfer of electrical charge between bodies upon contact and separation—is ubiquitous in natural and industrial processes, ranging from volcanic plumes [1], dust storms [2, 3], and coffee grinding [4] to pneumatic conveying [5], fluidized beds [6], and energy harvesting [7]. Despite centuries of study, the mechanisms of contact electrification remain incompletely understood [8], particularly for insulating materials [9].

Understanding contact electrification is challenging because it depends on many parameters. The role of most of these parameters, such as humidity [10, 11], flexoelectricity [12], the surrounding electric field [13, 14], surface roughness [15, 16], and turbulence [5, 17], has only recently begun to be clarified.

Nevertheless, despite stochastic variability and interference from other parameters, two principal relations of contact electrification between different materials were long considered established. First, the polarity of the impact charge was assumed to be governed by a material parameter, such as the contact potential difference. Second, the pre-impact charge of a particle was assumed to reduce the impact charge, leading the particle charge to converge to an equilibrium after repeated impacts. These relations form the basis of all theoretical models for particle charging upon impact on a different material, including the condenser model and its variants [18–21], the stochastic scaling model [22], and the mosaic model [23].

In contrast, experimental evidence for these relations is conflicting. Some experiments confirm them, showing that the impact charge of rubber and polymer particles decreases with increasing pre-impact charge, leading to convergence toward equilibrium [20, 24]. In others, the particle charge reverses polarity several times during the first few impacts before converging [25]. However, most

experiments on polymer particles show no influence of the pre-impact charge [26–28] or exhibit scatter too large to draw firm conclusions [29–33]. This scatter likely arises from simultaneous variations of parameters other than material and pre-impact charge, most commonly impact velocity and ambient conditions.

In some experimental campaigns, at least for a subset of tests, the particle impact charge increased with pre-impact charge [34–36]. This behavior is surprising because it implies divergent charging. In several cases, such divergence was attributed to other parameters affecting charge transfer, such as increased wall-normal velocity of highly charged particles, which enlarges the particle-surface contact area [37], polarization induced by surrounding charged particles [14], or particle size [38, 39]. Overall, the experimental evidence remains inconclusive. It is unclear whether deviations from charge convergence to a deterministic polarity result from interference with other parameters and whether isolated instances of divergent charging arise from intrinsic stochasticity.

To address this open question, we study contact electrification by single, well-controlled particle–target collisions. In these experiments, we keep all influential parameters, impact velocity, particle size, surface roughness, temperature, and humidity, constant and controlled as precisely as possible. We vary only the particle pre-impact charge and the particle and wall materials.

Using acoustic levitation, we suspend individual particles and release them to undergo a single, well-defined and repeatable impact with a target material (see Fig. 1a). Particles were collected from a low-density polyethylene (LDPE) storage bag and introduced into the acoustic levitator. Their initial charge, therefore, varied due to handling and, in some cases, was adjusted by corona discharge. Each experiment used a fresh particle from the same batch to avoid changes in surface roughness caused by repeated impacts [16].

The acoustic levitator traps a particle at pressure nodes of a standing acoustic wave between an ultrasonic

* holger.grosshans@ptb.de

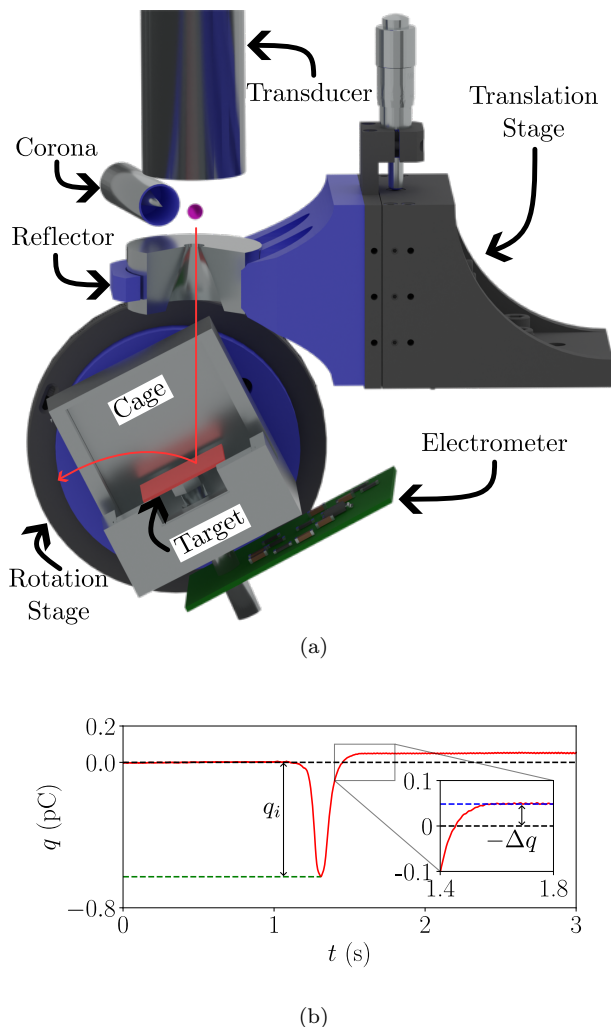


FIG. 1. (a) Schematic of the experimental apparatus and the levitated particle. (b) Example electrometer recording for a PS particle impacting a PTFE target. The red curve shows the charge signal (q) as a function of time (t) after background subtraction and correction for drift due to charge leakage (see End Matter for details). The levitator releases the particle at $t = 1.0$ s. The particle contacts the target at approximately $t = 1.3$ s, marked by the negative peak in the charge signal. The difference between the charge at release and at impact defines the particle’s pre-impact charge (q_i). After rebounding, the particle leaves the Faraday cage at approximately $t = 1.6$ s. The additive inverse of the difference between the charge at release and at exit from the Faraday cage defines the particle’s impact charge (Δq).

transducer and a reflective steel surface. The particle hovers above a small aperture in the reflector. Upon release, it passes through the aperture without contacting the edges, impacts a target positioned below, rebounds, and exits the enclosure. The target is fitted with interchangeable material caps that snap onto its base, ensuring impact with the selected material.

The target is connected to a custom-built electrometer that measures the charge induced on the target and

the surrounding cage with sub-femtocoulomb resolution. As illustrated by the exemplary impact of a polystyrene (PS) particle on a polytetrafluoroethylene (PTFE) target in Fig. 1b, the electrometer resolves the particle’s pre-impact charge (q_i) and the impact charge (Δq). The particle’s charge after impact is $q_i + \Delta q$.

All experiments were performed in a temperature- and humidity-controlled environment at 26 °C–27 °C and 12 %–13 % relative humidity. The apparatus was enclosed in a grounded metal housing to suppress external electromagnetic interference (EMI). Critical components were additionally shielded with conductive aluminum housings to minimize internal EMI.

A high-speed camera tracked the particle motion during impact. For each collision, we thus recorded the particle trajectory together with the pre-impact and impact charges.

Thus, the apparatus can keep all conditions fixed while varying only the particle and target materials and the particle’s pre-impact charge. Additional experimental details are provided in the End Matter.

First, we used this setup to study same-material contact charging. Specifically, we measured the impact charge of polymethyl methacrylate (PMMA) particles colliding with a PMMA target. The particle diameter, impact velocity, and regression results are summarized in Table I. Figure 2a plots the impact charge as a function of the pre-impact charge.

If the particle charge converged, particles with different pre-impact charges would evolve toward a common equilibrium value under repeated impacts. In that case, the regression line in Fig. 2a would have a negative slope. Instead, the regression has a positive slope. The pre-impact charge at which the impact charge vanishes, $q_{i,0} = 0.207$ pC for PMMA–PMMA, defines a divergence point. A positive slope implies that particles with any other pre-impact charge evolve away from this point after impact. Consequently, the absolute impact charge increases with the pre-impact charge for most values of q_i , except within the narrow interval between $q_i = 0$ pC and $q_{i,0}$.

The relative position of the pre-impact charge with respect to the divergence point determines the charging polarity. For $q_i > q_{i,0}$, the particle charges toward positive polarity, whereas for $q_i < q_{i,0}$ it charges toward negative polarity. Only in the small interval between $q_i = 0$ pC and $q_{i,0}$ does the impact charge oppose the pre-impact charge, allowing the particle polarity to reverse during impact.

Because Fig. 2a shows same-material charging, the impact charge exhibits substantial scatter, reflected by the low coefficient of determination (R^2) in Table I. To verify that the observed behavior is not due to random fluctuations in material parameters, we next investigate charging between different polymers.

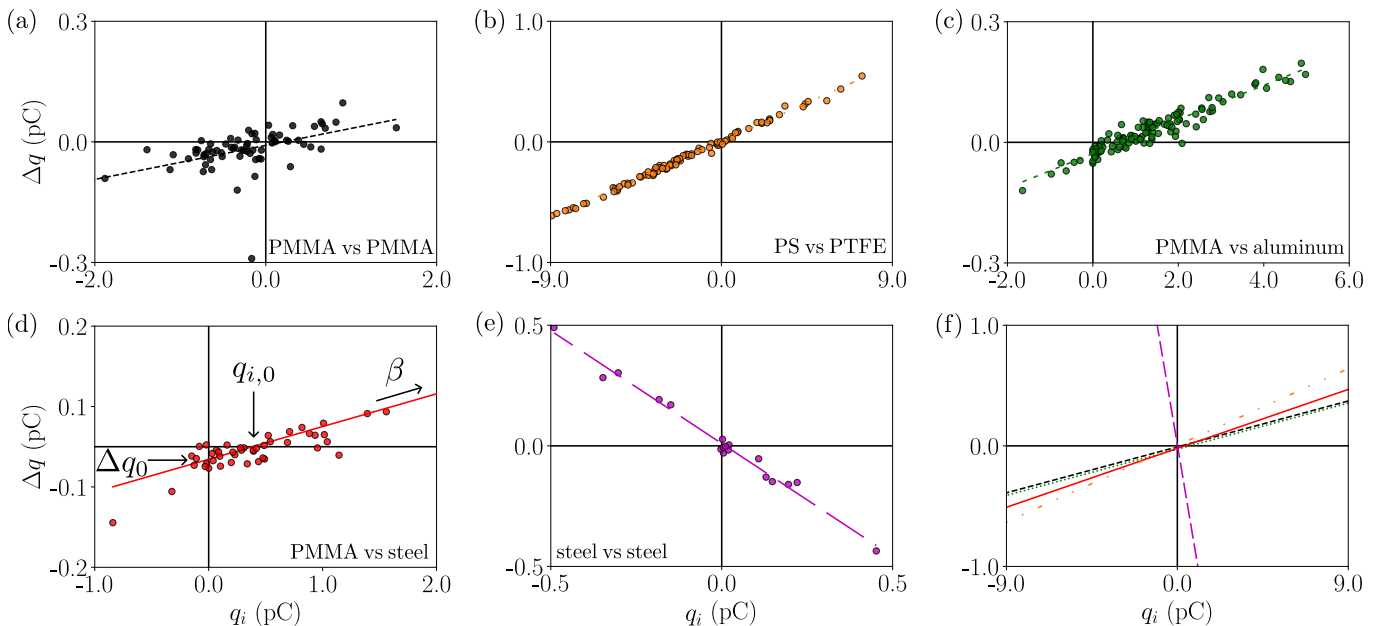


FIG. 2. Impact charge (Δq) against pre-impact charge (q_i). Impacts of (a) PMMA particles versus a PMMA target, (b) PS particles versus a PTFE target, (c) PMMA particles versus an aluminum target, (d) PMMA particles versus a steel target, and (e) steel particles versus a steel target. (f) Summary of the regression lines of (a)-(e). The impact charge of steel (conductive) particles converges, whereas the impact charge of all polymer (insulating) particles diverges.

TABLE I. Experimental conditions (particle diameter (d), normal impact velocity (v_n)) and parameters of the regression lines in Fig. 2 (slope (β), impact charge of an uncharged particle (Δq_0), divergence point ($q_{i,0}$), coefficient of determination (R^2)) with 95 % confidence interval.

Particle	Target	d (mm)	v_n (m/s)	β (pC/pC)	Δq_0 (pC)	$q_{i,0}$ (pC)	R^2
PMMA	PMMA	0.4	0.993 ± 0.006	0.042 ± 0.017	-0.009 ± 0.011	0.207 ± 0.010	0.26
PS	PTFE	1.0	1.230 ± 0.002	0.071 ± 0.001	0.004 ± 0.004	-0.061 ± 0.002	0.99
PMMA	aluminum	0.4	1.056 ± 0.011	0.043 ± 0.002	-0.028 ± 0.005	0.664 ± 0.003	0.91
PMMA	steel	0.4	1.019 ± 0.008	0.054 ± 0.028	-0.021 ± 0.020	0.384 ± 0.017	0.25
steel	steel	1.0	1.357 ± 0.014	-0.935 ± 0.061	0.010 ± 0.013	0.010 ± 0.030	0.98

Figure 2b shows the impact charge of PS particles colliding with a PTFE target as a function of pre-impact charge. Owing to their larger size, PS particles sustain higher charges and thus span a wider range of q_i . The regression slope is again positive, demonstrating divergent charging. The impact charge is fully determined by the pre-impact charge relative to the divergence point. Both positive and negative branches emerge symmetrically from this point. The high coefficient of determination excludes random scatter as the origin of the trend and confirms that the pre-impact charge controls the impact charge. Thus, the different-material impacts in Fig. 2b corroborate the same-material results in Fig. 2a.

To identify the material parameter responsible for divergent charging, we replace the insulating polymer target with conducting aluminum (Fig. 2c) and steel (Fig. 2d). For both conducting targets, the impact charge again scales linearly with the pre-impact charge with a positive slope, indicating divergence.

Last, we examine conductive particles impacting a conductive target: steel particles colliding with steel (Fig. 2e). Finally, the slope becomes negative. The slope close to -1 indicates that the particle loses nearly all of its pre-impact charge during impact. Thus, for steel-steel contacts, the impact charge drives the particle charge toward zero, corresponding to convergent charging.

The results in Fig. 2a-d demonstrate that particle impact charging can diverge. Because these experiments use isolated single particles shielded from external electric fields, this mechanism differs fundamentally from charge amplification in vibrating beds, which is driven by interparticle electric fields [14]. Comparison with Fig. 2e shows that the transition between divergent and convergent charging is governed by the particle material, most likely its electrical conductivity.

Figure 2f summarizes the regression curves for all experiments and highlights the contrast between insulating and conducting particles. All conducting particles exhibit similar slopes, independent of the specific particle

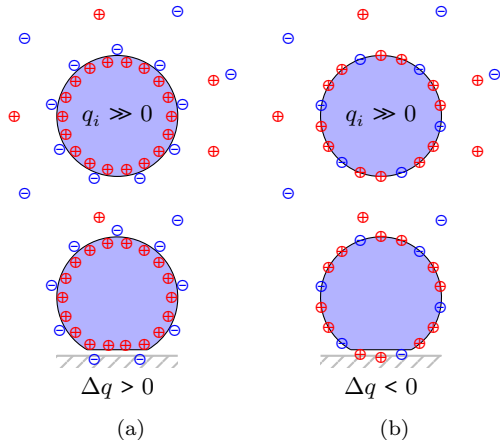


FIG. 3. Phenomenological explanation for (a) divergent charging of insulating and (b) convergent charging of conducting particles. Both particles have a positive pre-impact charge. The insulating particle loses negative charge during impact, thus obtaining a positive impact charge. The insulating particle loses positive charge during impact, thus obtaining a negative impact charge.

or target material. This universality implies that the impact charge is governed by a single material parameter shared by the experiments in Fig. 2a-d and distinct from that in Fig. 2e. This observation again points to particle conductivity.

Contrary to the slope, the impact charge at zero pre-impact charge depends on the material combination, as summarized in Table I. For same-material charging (PMMA–PMMA and steel–steel) and for similar materials (PS–PTFE), Δq_0 is small. For dissimilar materials (PMMA–aluminum and PMMA–steel), Δq_0 is significantly larger. Because the pre-impact charge vanishes, these results indicate that Δq_0 arises from a triboelectric mechanism governed by the material combination.

Based on these observations, we propose a phenomenological model, sketched in Fig. 3, for convergent and divergent impact charging. Consistent with existing theories, we decompose the total impact charge into a triboelectric contribution Δq_0 and a term proportional to the pre-impact charge,

$$\Delta q = \Delta q_0 + \beta q_i. \quad (1)$$

For $\beta < 0$, the particle charge converges; for $\beta > 0$, it diverges.

For insulating particles, we assume two distinct charge locations and mechanisms in which the particle holds pre-impact charge. First, a bound charge, for example, associated with oxidized polymer chains exposed to ambient air (\oplus inside the particle in Fig. 3a). The bound charge remains fixed due to its low conductivity.

Second, a loosely bound surface charge consisting of adsorbed free ions from the surrounding atmosphere

(\ominus at the particle’s surface in Fig. 3a). The particle attracts ions of opposite polarity to its bound charge. The higher q_i , the more ions the particle attracts. Nevertheless, the amount of adsorbed charge remains small compared to the bound charge; otherwise, the net pre-impact charge would vanish. Because these ions are weakly bound and located at the surface, they dominate the charge transfer that depends on q_i . Accordingly, for insulating particles,

$$0 < \beta \ll 1. \quad (2)$$

For conductive particles, charge carriers are mobile over the surface. Adsorbed ions and pre-impact charge therefore blend (Fig. 3b), and the charge density at the contact region is dominated by the pre-impact charge. If the surface charge relaxation time is short compared to the contact time, the slope approaches $\beta \approx -1$. Thus, β is a function of the particle material’s conductivity.

The observation of divergent impact charging for polymer particles is unexpected. Motivated by this finding, we reexamine previously published measurements [33]. Figure 4a reproduces the original impact charge and pre-impact charge data for 200 μm PMMA particles, which appear randomly scattered. These data were obtained from a cascade experiment in which particles undergo multiple impacts between parallel steel plates at decreasing impact velocities.

We reprocess the data by filtering for similar impact velocities. Figure 4b includes only impacts with normal velocities between 30 m/s and 50 m/s, while Fig. 4c includes impacts above 50 m/s. After filtering, the particle charge clearly diverges, consistent with our present measurements.

Figure 4d shows two representative charge trajectories as a function of impact number n . One particle has a positive charge before the first impact and evolves toward a positive equilibrium. The other has a negative charge before the first impact and evolves toward a negative equilibrium. These two examples are representative of the complete re-evaluated dataset. Although the quantitative charge evolution differs, all share the same qualitative behavior: The polarity before the first impact determines the polarity toward which the particle evolves.

Figure 4d also shows the impact charge evolution for the positively charging particle. The pre-impact charge before the second impact exceeds that before the first, and the corresponding impact charge is larger, consistent with Eq. (2). At later stages, the relation between Δq and q_i reverses, indicating that additional mechanisms, such as charge relaxation [40], limit further charging near equilibrium. This regime lies outside the scope of the experiments analyzed in Fig. 2.

Other previously reported measurements can be reinterpreted in a similar way. For example, impact charges of PS particles on aluminum measured by Korevaar [41]

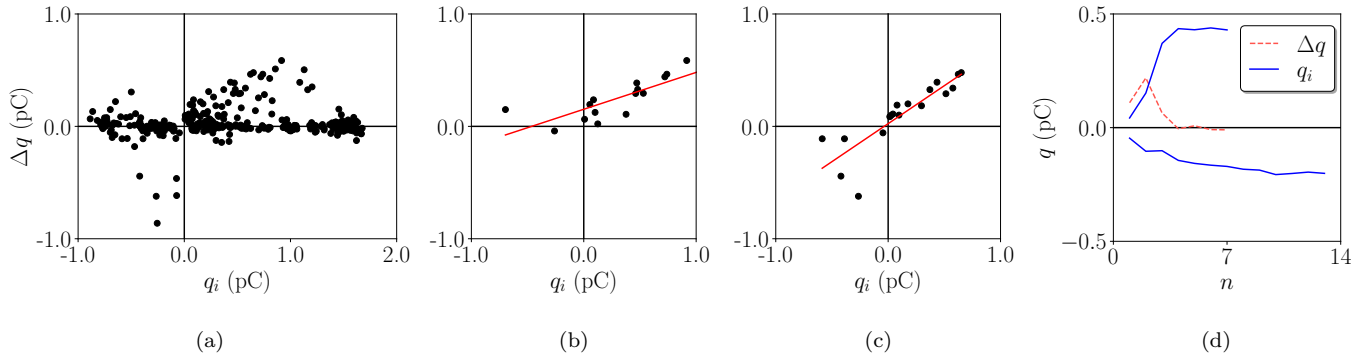


FIG. 4. Impact charge (Δq) of 200 μm -sized PMMA particles in a cascade experiment. Each particle undergoes several successive impacts on steel plates at decreasing velocity. (a) Originally published scattered impact-charge distribution [33]. The impact charges filtered for normal velocities between (b) 30 m/s and 50 m/s and (c) above 50 m/s diverge. (d) Particle charge versus impact number (n) for two individual particles. One starts positively charged and remains positive; the other starts negatively charged and remains negative throughout subsequent impacts.

appear to decrease with increasing pre-impact charge. However, when the data are filtered by impact number, which correlates with normal impact velocity, each subset exhibits a positive slope.

In summary, our experiments and reanalysis of prior data demonstrate a divergent impact charging of insulating particles, in which the impact charge increases linearly with the pre-impact charge. The polarity of the charge evolution is determined by the pre-impact charge relative to the divergence point. This behavior contradicts existing particle charging models. We propose a phenomenological explanation based on the adsorption of surface ions with polarity opposite to the particle's pre-impact charge, which dominate charge transfer during impact.

Acknowledgments—This project has received funding from the European Research Council (ERC) under the European Union's Horizon 2020 research and innovation programme (grant agreement No. 947606 PowFEct) and the Deutsche Forschungsgemeinschaft (DFG, German Research Foundation) – Projektnummer 562343622.

Data availability—The design, manufacturing files of the amplifier, and control scripts can be accessed via https://gitlab1.ptb.de/asep/charge_amplifier. Raw data from the experiments are available from the authors upon reasonable request.

[1] C. Cimarelli and K. Genareau, A review of volcanic electrification of the atmosphere and volcanic lightning, *J. Volcanol. Geothermi. Res.* **422**, 107449 (2022).
 [2] A. K. Kamra, Physical sciences: Visual observation of electric sparks on gypsum dunes, *Nature* **240**, 143 (1972).

[3] T. Shinbrot, K. LaMarche, and B. J. Glasser, Triboelectrification and razorbacks: Geophysical patterns produced in dry grains, *Phys. Rev. Lett.* **96**, 178002 (2006).
 [4] J. Méndez Harper, C. S. McDonald, E. J. Rheingold, L. C. Wehn, R. E. Bumbaugh, E. J. Cope, L. E. Lindberg, J. Pham, Y.-H. Kim, J. Dufek, and C. H. Hendon, Moisture-controlled triboelectrification during coffee grinding, *Matter* **7**, 266 (2024).
 [5] S. Jantač and H. Grosshans, Suppression and control of bipolar powder charging by turbulence, *Phys. Rev. Lett.* **132**, 054004 (2024).
 [6] A. Giffin and P. Mehrani, Effect of gas relative humidity on reactor wall fouling generated due to bed electrification in gas-solid fluidized beds, *Powder Technol.* **235**, 368 (2013).
 [7] A. Šutka, L. Lapčinskis, D. He, H. Kim, J. D. Berry, J. Bai, M. Knite, A. V. Ellis, C. K. Jeong, and P. C. Sherrell, Engineering polymer interfaces: A review toward controlling triboelectric surface charge, *Adv. Mater. Interfaces* **10**, 2300323 (2023).
 [8] D. J. Lacks and T. Shinbrot, Long-standing and unresolved issues in triboelectric charging, *Nat. Rev. Chem.* **3**, 465 (2019).
 [9] K. Sotthewes, H. J. G. E. Gardeniers, G. Desmet, and I. S. M. Jimidar, Triboelectric charging of particles, an ongoing matter: From the early onset of planet formation to assembling crystals, *ACS Omega* **7**, 41828 (2022).
 [10] A. Crovetto, H. Hempel, M. Rusu, L. Choubrac, D. Kojda, K. Habicht, and T. Unold, Water adsorption enhances electrical conductivity in transparent p-type cui, *ACS Appl. Mater. Interfaces* **12**, 48741 (2020).
 [11] N. Amieur, Z. Ziari, and S. Sahli, Traps energy distribution in Kapton HN polyimide films through surface potential decay model under humidity conditions, *J. Electrostat.* **109**, 103551 (2021).
 [12] C. A. Mizzi, A. Y. W. Lin, and L. D. Marks, Does flexoelectricity drive triboelectricity?, *Phys. Rev. Lett.* **123**, 116103 (2019).
 [13] T. Siu, J. Cotton, G. Mattson, and T. Shinbrot, Self-sustaining charging of identical colliding particles, *Phys. Rev. E* **89**, 052208 (2014).

- [14] R. Yoshimatsu, N. A. M. Araújo, G. Wurm, H. J. Herrmann, and T. Shinbrot, Self-charging of identical grains in the absence of an external field, *Sci. Rep.* **7**, 39996 (2017).
- [15] S. Jantač, J. Pelcová, J. Sklenářová, M. Drápela, H. Grosshans, and J. Kosek, Triboelectric charging model for particles with rough surfaces, *Adv. Powder Technol.* **36**, 104787 (2025).
- [16] J. C. Sobarzo, F. Pertl, D. M. Balazs, T. Costanzo, M. Sauer, A. Foelske, M. Ostermann, C. M. Pichler, Y. Wang, Y. Nagata, M. Bonn, and S. Waitukaitis, Spontaneous ordering of identical materials into a triboelectric series, *Nature* **638**, 664 (2025).
- [17] G. Ozler and H. Grosshans, Secondary flows drive triboelectric powder charging in pneumatic conveying, *J. Fluid Mech.* **1007**, A52 (2025).
- [18] W. John, G. Reischl, and W. Devor, Charge transfer to metal surfaces from bouncing aerosol particles, *J. Aerosol Sci.* **11**, 115 (1980).
- [19] J. Laurentie, P. Traoré, and L. Dascalescu, Discrete element modeling of triboelectric charging of insulating materials in vibrated granular beds, *J. Electrostat.* **71**, 951 (2013).
- [20] S. Matsusaka, M. Ghadiri, and H. Masuda, Electrification of an elastic sphere by repeated impacts on a metal plate, *J. Phys. D Appl. Phys.* **33**, 2311 (2000).
- [21] C. Pei, C.-Y. Wu, D. England, S. Byard, H. Berchtold, and M. Adams, Numerical analysis of contact electrification using DEM-CFD, *Powder Technol.* **248**, 34 (2013).
- [22] H. Grosshans, G. Ozler, V. Veeravalli, and S. Jantač, Unifying same- and different-material particle charging through stochastic scaling, *Phys. Rev. X*, (2025).
- [23] G. Grosjean and S. Waitukaitis, Asymmetries in triboelectric charging: Generalizing mosaic models to different-material samples and sliding contacts, *Phys. Rev. Mater.* **7**, 065601 (2023).
- [24] C. Han, Q. Zhou, J. Hu, C. Liang, X. Chen, and J. Ma, The charging characteristics of particle–particle contact, *J. Electrostat.* **112**, 103582 (2021).
- [25] M. Kaponig, A. Mölleken, H. Nienhaus, and R. Möller, Dynamics of contact electrification, *Sci. Adv.* **7**, eabg7595 (2021).
- [26] G. Grosjean and S. Waitukaitis, Single-collision statistics reveal a global mechanism driven by sample history for contact electrification in granular media, *Phys. Rev. Lett.* **130**, 098202 (2023).
- [27] P. M. Ireland, Impact tribocharging of soft elastic spheres, *Powder Technol.* **348**, 70 (2019).
- [28] A. G. Kline, M. X. Lim, and H. M. Jaeger, Precision measurement of tribocharging in acoustically levitated submillimeter grains, *Rev. Sci. Instrum.* **91**, 023908 (2020).
- [29] T. Matsuyama, M. Ogu, H. Yamamoto, J. C. M. Marijnissen, and B. Scarlett, Impact charging experiments with single particles of hundred micrometre size, *Powder Technol.* **135–136**, 14 (2003).
- [30] L. Konopka, S. Jantač, M. Vrzáček, M. Svoboda, and J. Kosek, Triboelectric charging of polyethylene powders: Comparison of same-material and different-material contributions to the charge build-up, *Powder Technol.* **367**, 713 (2020).
- [31] A. Schella, S. Herminghaus, and M. Schröter, Influence of humidity on tribo-electric charging and segregation in shaken granular media, *Soft Matter* **13**, 394 (2017).
- [32] S. Jantač, L. Konopka, and J. Kosek, Experimental study of triboelectric charging of polyethylene powders: Effect of humidity, impact velocity and temperature, *Adv. Powder Technol.* **30**, 148 (2019).
- [33] H. Grosshans, W. Xu, and T. Matsuyama, Simulation of pmma powder flow electrification using a new charging model based on single-particle experiments, *Chem. Eng. Sci.* **254**, 117623 (2022).
- [34] F. Chowdhury, M. Ray, A. Passalacqua, P. Mehrani, and A. Sowinski, Electrostatic charging due to individual particle-particle collisions, *Powder Technol.* **381**, 352 (2021).
- [35] F. Chowdhury, B. Elchamaa, M. Ray, A. Sowinski, A. Passalacqua, and P. Mehrani, Apparatus design for measuring electrostatic charge transfer due to particle-particle collisions, *Powder Technol.* **361**, 860 (2020).
- [36] O. Obukohwo, S. Jantač, A. Sowinski, P. Mehrani, and H. Grosshans, A novel apparatus for particle-particle single contact electrification experiments, *Powder Technol.* **accepted** (2026).
- [37] H. Grosshans and M. V. Papalexandris, A model for the non-uniform contact charging of particles, *Powder Technol.* **305**, 518 (2016).
- [38] K. M. Forward, D. J. Lacks, and R. M. Sankaran, Charge segregation depends on particle size in triboelectrically charged granular materials, *Phys. Rev. Lett.* **102**, 028001 (2009).
- [39] T. F. O’Hara, D. P. Reid, G. L. Marsden, and K. L. Aplin, Faraday cup measurements of triboelectrically charged granular material: a modular interpretation methodology, *Soft Matter* **21**, 855 (2025).
- [40] T. Matsuyama and H. Yamamoto, Maximum electrostatic charge of powder in pipe flow, *Adv. Powder Technol.* **21**, 350 (2010).
- [41] M. Korevaar, *Particles in charge: An experimental and numerical study on the tribo-electric charging of pneumatically conveyed powders* (Technische Universiteit Eindhoven, 2016).
- [42] N. Pérez, M. A. B. Andrade, R. Canetti, and J. C. Adamowski, Experimental determination of the dynamics of an acoustically levitated sphere, *J. Appl. Phys.* **116**, 184903 (2014).
- [43] J. C. Crocker and D. G. Grier, Methods of digital video microscopy for colloidal studies, *J. Colloid Interface Sci.* **179**, 298 (1996).

END MATTER

Acoustic Levitation—The acoustic trap consists of a standing acoustic wave between an ultrasonic transducer (Hielscher UIP 500hdT with BS4d22 and BS4-2.2 adapters) and a steel reflector, as shown in Fig. 5a. The transducer amplifies vibrations of a piezoelectric stack resonating between 19.38 kHz and 19.42 kHz, depending on temperature and atmospheric pressure. The transducer–reflector spacing is set to an integer multiple of half the acoustic wavelength. The transducer is rigidly fixed to the apparatus frame. Fine alignment of the reflector is achieved using a ThorLabs three-axis translation stage combined with a two-axis rotation stage.

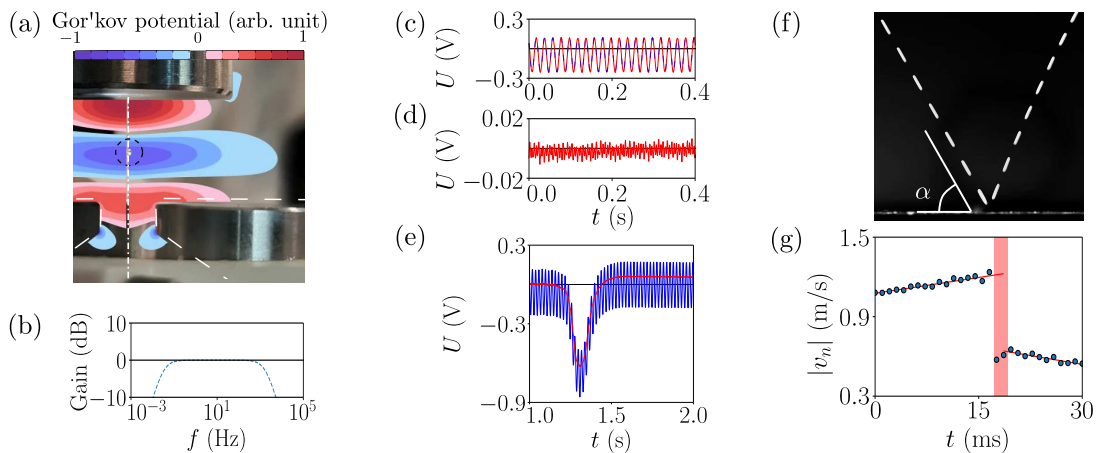


FIG. 5. Details of the experimental apparatus. (a) Gor'kov potential of the standing acoustic wave that traps the particle. (b) Unity-gain response of the analog section for sampling frequencies up to 1 kHz. (c) Red: raw electrometer signal during the first 0.4 s; blue: fitted 50 Hz grid-noise component using Eq. (4). (d) Signal after subtraction of the 50 Hz component. (e) Blue: raw electrometer signal after 1.0 s; red: filtered signal with grid noise removed. (f) Time-lapse composite of a particle collision. (g) Particle velocity before and after impact (red bar) as a function of the time since entering the camera window.

Because the diameter of the largest particle used (1.0 mm) is less than one tenth of the acoustic wavelength, the trapping potential is well described by the Gor'kov potential [42],

$$U_G = \frac{\pi}{4} d^3 \left(\frac{p_{\text{rms}}^2}{3\rho_f c_f^2} - \frac{\rho_f v_{\text{rms}}^2}{2} \right). \quad (3)$$

Here, p_{rms} is the root-mean-square pressure, ρ_f the fluid density, c_f the speed of sound, and v_{rms} the root-mean-square wave velocity. Small particles are trapped in the resulting potential well, enabling stable levitation even for dense metallic particles, as illustrated in Fig. 5a.

The particle is levitated above a circular aperture in the reflector. The aperture is sufficiently small not to perturb the acoustic potential, yet large enough to allow the particle to pass through without contacting the reflector upon release.

Charge Measurement—After release, the particle falls through the aperture, impacts the target inside the Faraday cage, and rebounds. The target is electrically connected to the Faraday cage but insulated from the rotational stage by a dielectric adapter. Immediately before impact, the charged particle induces an equal and opposite charge on the Faraday cage, corresponding to the additive inverse of the pre-impact charge (Fig. 1b). After the particle exits the cage, the additive inverse of the impact charge remains on the target (Fig. 1b).

A custom-built electrometer connected to the Faraday cage converts the induced charge into a voltage signal, which is digitized and recorded for post-processing. The electrometer comprises an analog section mounted directly on the Faraday cage and a digital/power section located behind an external EMI shield. The analog

section consists of two inverting amplifier stages. The first stage uses a Texas Instruments LMP7721 operational amplifier with a 1 nF feedback capacitor to integrate the induced current. The second stage uses a Texas Instruments OPA2211 amplifier to amplify the signal by a factor of 1000 and invert it. The amplified signal is transmitted via a shielded cable to the digital section, where it is digitized by a 16-bit analog-to-digital converter (Texas Instruments ADS8513). An Arduino microcontroller timestamps the data and transmits it to a PC via USB.

This configuration achieves a charge resolution of 0.6 fC and a sampling interval of 0.5 ms. The analog section exhibits unity gain (0 dB) for sinusoidal input signals of 1 pC up to frequencies of 1 kHz, as shown in Fig. 5b. The lower unity-gain cutoff is approximately 0.1 Hz and can be extended through post-processing correction of leakage currents.

The raw electrometer signal contains a pronounced 50 Hz component originating from the European power grid. Because the grid period is comparable to the particle residence time within the Faraday cage, conventional filtering is ineffective. Instead, we exploit the linear superposition of electric fields and subtract the grid-induced component from the signal. To this end, we record the electrometer output for one second prior to particle release (see Fig. 1b, Fig. 5c and d) and fit the data to

$$V(t) = a \sin(\omega t + \varphi) + V_0, \quad (4)$$

where a is the amplitude, ω the angular frequency, φ the phase, and V_0 the offset. The fitted component is then subtracted from the full signal.

Figure 5e shows a representative example. The grid-noise amplitude is reduced from 172 mV to 6 mV. The

remaining noise is predominantly high-frequency and is further suppressed by convolving with a 3.5 ms window function, chosen to preserve the particle-induced signal.

We finally correct for leakage currents, which are dominated by the feedback resistor of the first amplifier stage. The leakage contribution is given by

$$\dot{V}_{\text{leak}}(t) = -\frac{V_{\text{con}}(t)}{k}, \quad (5)$$

where $k = RC = 4.9$ s is the leakage constant and $V_{\text{con}}(t)$ the convolved signal. The corrected voltage is obtained as

$$V_{\text{cor}}(t) = V(t) + \int_0^t \Delta \dot{V}_{\text{leak}} dt. \quad (6)$$

The electrometer output is calibrated to 1 V per 1 pC. After correction, we extract the pre-impact and impact charges. Calibration against a Keithley 6517B electrome-

ter using a Monroe Electronics Faraday cup shows agreement within 2 % over the full measurement range.

Impact Tracking—Particle motion during impact is recorded using a high-speed camera (Mikrotron Quad GigE) equipped with a macro lens (Laowa 100 mm f/2.8 2× Ultra Macro APO), as shown in Fig. 5f. From the recordings, we determine particle position, impact velocity, and impact angle.

Background subtraction is performed using singular value decomposition. The frames are then rotated so that the target edge aligns with the image baseline. Particle positions and trajectories are identified using the TrackPy package [43]. As illustrated in Fig. 5g, we identify the collision frame and fit linear trajectories to the normal pre- and post-impact motion to extrapolate the impact velocity, v . Frames for which the velocity cannot be reliably estimated, marked by the vertical red bar in Fig. 5g, are excluded from the fit.

The impact angle α is obtained by extrapolating the trajectory to the collision point and measuring the angle of incidence. The normal impact velocity is $v_n = v \sin \alpha$.